

Multi-wavelength observations of serendipitous *Chandra* X-ray sources in the field of A 2390

C.S. Crawford¹, P. Gandhi¹, A.C. Fabian¹, R.J. Wilman^{1,2}, R.M. Johnstone¹, A.J. Barger^{3,4,5,6} and L.L. Cowie^{3,6}

1. Institute of Astronomy, Madingley Road, Cambridge CB3 0HA

2. Leiden Observatory, P.O. Box 9513, 2300 RA Leiden, The Netherlands

3. Institute for Astronomy, 2680 Woodlawn Drive, Honolulu HI 96822, USA

4. Dept. of Astronomy, University of Wisconsin-Madison, 475 N Charter Street, Madison, WI 53706 USA

5. Hubble Fellow and Chandra Fellow at Large

6. Visiting Astronomer, W.M. Keck Observatory, jointly operated by the California Institute of Technology and the University of California

16 November 2018

ABSTRACT

We present optical spectra and near-infrared imaging of a sample of serendipitous X-ray sources detected in the field of *Chandra* observations of the A 2390 cluster of galaxies. The sources have 0.5–7 keV fluxes of $0.6 - 8 \times 10^{-14} \text{ erg cm}^{-2} \text{ s}^{-1}$ and lie around the break in the 2–10 keV source counts. They therefore are typical of sources dominating the X-ray Background in that band. Twelve of the fifteen targets for which we have optical spectra show emission lines, most of which have soft X-ray spectra. Including photometric redshifts and published spectra we have redshifts for seventeen of the sources, ranging from $z \sim 0.2$ up to $z \sim 3$ with a peak between $z = 1 - 2$. Ten of our sources have hard X-ray spectra indicating a spectral slope flatter than that of a typical unabsorbed quasar. Two hard sources that are gravitationally lensed by the foreground cluster are obscured quasars, with intrinsic 2–10 keV luminosities of $0.2 - 3 \times 10^{45} \text{ erg s}^{-1}$ and absorbing columns of $N_{\text{H}} > 10^{23} \text{ cm}^{-2}$. Both were detected by ISO, showing that the absorbed flux emerges in the far-infrared.

Key words:

diffuse radiation – X-rays: galaxies – infrared: galaxies – galaxies: active

1 INTRODUCTION

The cosmic X-ray Background (XRB) in the energy range 0.5–7 keV has now been mostly resolved into point sources. About 90 per cent of the 0.5–2 keV soft XRB has been resolved with *ROSAT* (Hasinger et al 1998; Lehmann et al 2001), and now *Chandra* has also resolved more than 80 per cent of the harder 2–7 keV band (Mushotzky et al 2000; Hornschemeier et al 2001; Giacconi et al 2001; Barger et al 2001; Tozzi et al 2001; Brandt et al 2001). Follow-up work on the deep fields which gave these *Chandra* results is proceeding but full details including redshifts are only published for about a half, or less, of the brighter sources detected. The determination of complete details of the optically and X-ray faintest sources is likely to take some time.

The harder 2–7 keV X-ray source counts flatten below a flux of about $10^{-14} \text{ erg cm}^{-2} \text{ s}^{-1}$ (Mushotzky et al 2000; Giacconi et al 2001), which means that much of the information about the origin of the bulk of the XRB is contained in sources around that flux level. Deep X-ray observations are not required to detect such sources and several tens are routinely found as serendipitous sources in *Chandra* exposures of 10–20 ks on other targets. Indeed, for a given total exposure time, more such sources are found from

say 10 separate 20 ks exposures than will be found from one deep 200 ks exposure, due to the flatter faint source counts.

We have begun a programme (Fabian et al 2000; Crawford et al 2001) of studying the serendipitous sources in our *Chandra* cluster fields, which have typical exposures of about 20 ks. At this flux level the optically-identified sources are associated roughly equally with normal quasars, optically-bright galaxies and optically-faint galaxies (Mushotzky et al 2000). The latter often appear to be of early-type (Barger et al 2001). All are plausibly powered by active galactic nuclei (AGN), but the harder sources are mostly obscured by significant intrinsic absorption columns ($\sim 10^{21} - 10^{23} \text{ cm}^{-2}$). Reddening by dust associated with this absorbing gas can render the AGN itself undetectable at optical and near-infrared wavelengths. Obscured AGN plausibly explain the spectral shape of the XRB (Setti & Woltjer 1989; Madau, Ghisellini & Fabian 1994; Comastri et al 1995).

Here we report on the field of the cluster A 2390 (Fabian et al 2000; Allen, Ettori & Fabian 2001; Cowie et al 2001), where we detect 31 serendipitous sources in two separate *Chandra* observations totalling about 19 ks. Two have stellar optical spectra and of the remaining 21 optical identifications we have measured spectroscopic

redshifts for 13 and obtain photometric redshifts from optical and near-infrared images of a further 4. We test the photometric redshift approach for such sources against the spectroscopic results where both are available. The resulting redshift distribution stretches out to $z \sim 3$ with a peak between $z = 1 - 2$. Ten of our sources have hard X-ray spectra indicating a spectral slope flatter than that of a typical unabsorbed quasar. X-ray spectral fitting has been carried out on the 8 brightest sources. Some X-ray variability is detected between the two observations.

Strong gravitational lensing has enhanced three sources. These were also detected by ISO in its deepest exposure, which was of A 2390 (Altieri et al. 1999). Two of these appear to be genuine obscured quasars.

2 OBSERVATIONS AND RESULTS

2.1 Detection of the X-ray serendipitous sources

The $z = 0.228$ cluster A 2390 was observed on two occasions with the *Chandra* X-ray observatory: on 2000 October 08 (with sequence number 800008 and focal plane temperature of -120°C) for 9.83 ks; and on 1999 November 05 (seq. no. 800009 and focal plane temperature of -110°C) for 9.13 ks. The analysis of the X-ray emission from A 2390 itself is published elsewhere (Allen, Etti & Fabian 2001); here we investigate the properties of the serendipitous point sources identified in the field. For each observation, the cluster was placed ~ 1 arcmin from the centre of chip ACIS-S3, and five of the chips (ACIS-23678) were operating. The roll angle differed only slightly between the two observations (-171° for 800008, -190° for 800009), so there is a large overlap between their fields of view.

The 800009 dataset was updated for the correct gainfile (as of 2000 October). The lightcurve of the S3 data showed no evidence for flaring of the background level during either observation, so we use the data from the full duration of each exposure. The data were exposure-map corrected to account for the decrease in effective area off-axis. We did not attempt to mitigate the charge transfer inefficiency, or filter on event grades, as we wished to retain the option of extracting and fitting to an X-ray spectrum of the brighter sources.

We searched the total *Chandra* field of view for serendipitous sources using the Chandra Interactive Analysis of Observations (CIAO) WAVDETECT detection algorithm. WAVDETECT was run on the data from each chip in the 0.5-7 keV band, with the data at three binnings: the original unbinned pixels (each of 0.5 arcsec), and binned by two and four pixels (ie 1 and 2 arcsec bins respectively). We find this is an efficient way of detecting the widest range of sources, as the best precision can be obtained for most sources from the unbinned image, but the fainter or more diffuse sources (especially in chips where the point spread function (PSF) is more extended) only appear significant at higher binnings. We experimented with a full range of wavelet scales (using the $\sqrt{2}$ sequence of 1, 1.414, 2.0 ... 16.0 pixels) to pick up different sized sources, and set the significance threshold for sources at 10^{-5} for the 2-pixel binning, and at 10^{-6} for the 1-pixel binning and unbinned data.

We discarded all sources with fewer (non-background subtracted) than 10 counts as too marginal, and any found within 20 arcsec of the edge of each chip. The spacecraft dither is on this scale, and so there is a danger that some of the counts for sources too near the chip edge will be lost during the observation. Each

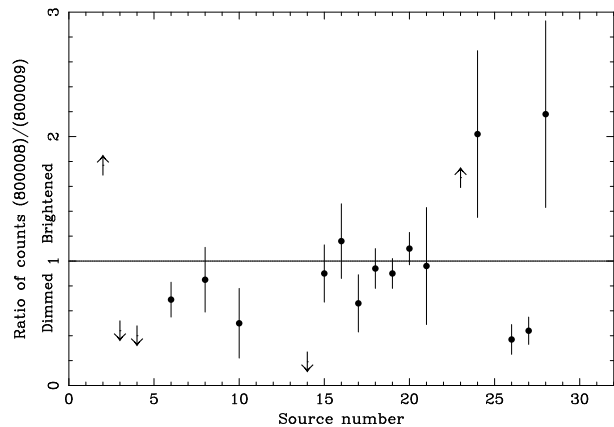


Figure 1. The ratio of counts in the serendipitous sources in common between 800009 (earlier) and the 800008 (later) observations. One- σ errors are shown on the ratios.

source was examined by eye, in order to discard any that could be due to the prominent stripes apparent in the background of some of the chips. These stripes appear at soft energies, and are most noticeable in chip ACIS-S4, and we only include one (totally unambiguous) source from this chip (A12). Other chips marginally affected by background stripes are chips I2, I3 and S2 in the 800009 observation. We end up with a total of 31 serendipitous sources, and they are listed in Table 1. The first dataset (800009) was observed when the registration between the *Chandra* coordinates and the real Sky was incorrect. We have corrected for this using the 12 sources that were detected in common between the two separate observations. All the coordinates given for the 800009 dataset in Table 1 have been corrected for this ~ 2 arcsec offset.

We also estimated the counts in each source in 3 energy bands: 0.5-2 keV (soft), 2-7 keV (hard) and 0.5-7 keV (total). The counts were taken from a box centred around a source, with a length given by the square root of the number of pixels in the source cell (as given from WAVDETECT). The local background was estimated from a concentric box with a length five times longer. The background box was offset if it would otherwise spill over the edge of the chip, or would include a close neighbouring source. Where the source counts (in any band) were less than twice the error on that value, we replaced the value with an upper limit set at twice the error. For nearly all the sources the counts obtained from WAVDETECT and our box statistics agree within the errors. The only major exceptions are sources A1 – the most off-axis, and a very diffuse source – and A22, which is perhaps rather close to the edge of the chip. We used the background-subtracted counts in the hard and soft bands to estimate a soft-to-hard ratio (S/H) for each source. The higher sensitivity of *Chandra* below 2 keV means that even genuinely hard sources can still show plenty of counts in our soft band (see eg Crawford et al. 2001). The WAVDETECT results, counts for each source in the different bands and the S/H ratio are presented in Table 1. A few of the sources also varied significantly in brightness over the 11 months between the two observations. Specifically, sources A2 and A23 brightened over this period, whilst A3, A4, A6, A14, A26 and A27 all faded (Fig 1). The colours of A6 and A27 also appeared to soften appreciably over this period.

Our faintest sources typically have 10-11 counts over the full 0.5-7 keV energy range; 10 counts corresponds to count-rates of $1.017 \times 10^{-3} \text{ ct s}^{-1}$ in the 800008 observation and $1.095 \times 10^{-3} \text{ ct s}^{-1}$ for the 800009 observation. Assuming a power law model with slope $\Gamma = 1.4$ (similar to the slopes we find

when modelling the spectra of our brighter sources; see section 2.5), that is absorbed only by the Galactic column ($\sim 6.81 \times 10^{20} \text{ cm}^{-2}$ in this direction; Stark et al 1992) we use PIMMS to translate source counts into fluxes. A source with a countrate of $10^{-3} \text{ ct s}^{-1}$ observed in a back-illuminated chip (S1 or S3) is predicted to have a (0.5-7 keV) flux of $6.7 \times 10^{-15} \text{ erg cm}^{-2} \text{ s}^{-1}$. If observed in a front-illuminated chip this countrate corresponds to $1.1 \times 10^{-14} \text{ erg cm}^{-2} \text{ s}^{-1}$.

2.2 Infra-red and optical photometry

We reduced optical images of the field around A 2390 available from the archives of the Isaac Newton Group telescopes, and the Canada-France-Hawaii Telescope. Where the position of a serendipitous source was not covered in the field of view of one of the archival datasets, we used the Digitized Sky Survey (DSS; second generation) images. The optical data enabled us to preferentially select sources with no, or a faint, optical identification as most suitable for imaging in the near-infrared. J, H and K photometry of twelve of the serendipitous sources from the 800009 observation was obtained on the nights of 2000 August 10 and 11 at the United Kingdom Infrared Telescope (UKIRT), using the UFTI full-array with a 92 arcsec field of view. A summary of the observations (archival and dedicated) taken are shown in Table 2. The optical data were flux-calibrated using standard Landolt stars, except for the CFHT *I*-band data, which was cross-calibrated from the flux-calibrated WHT *I*-band image. The standards for the infra-red data were taken from the UKIRT faint-star catalogue.

Magnitudes of the sources were obtained using PHOT in IRAF, using a consistent aperture in all the bands in order to provide accurate colours for later user in photometric redshift fitting. Since the seeing for the *B*-band was very large, a typical aperture of 4.5 arcsec diameter was chosen for most objects, except for some of the very faint ones and for objects with close neighbours, for which an aperture of 2.7 arcsec diameter was chosen, and seeing correction performed in all the bands. The optical and infra-red magnitudes are listed in Table 3. Since this is a crowded field, a very large sky aperture was used estimate the background, relying on PHOT K-sigma clipping to remove any sources in the background box. A limiting magnitude was estimated for each source as the $3\text{-}\sigma$ sky standard deviation multiplied by the square-root of the number of good pixels in the object aperture. The infra-red images were typically uncrowded and background estimation could be performed with apertures that did not typically include other sources. The magnitudes for our sources agree well with the magnitudes obtained by Cowie et al. (2001) when account is taken of the fact that the apertures we use are large (typically a diameter of 4.5 arcsec to encompass the poor PSF in the optical) as compared to 2 arcsec diameter used in Cowie et al.

2.3 Optical spectroscopy

We took optical spectra of fifteen of the serendipitous background sources listed in Table 1; the selection of which sources to observe was fairly random, with a preference only for those with definite optical identifications, and which were least off-axis in the *Chandra* observations. The spectra were taken on 2000 September 28 and 29 with the Keck Echelette Spectrograph and Imager (ESI; Epps & Miller 1998) used in low resolution mode with a 1 arcsec slit. The nights were photometric with seeing of about 0.7 arcsec. Targets were observed at three positions along the slit with 600 sec exposure times at each position and the median of the observations used

to form the sky. The observations were then sky subtracted, aligned, and the spectrum extracted. The wavelength calibration was determined from the night sky emission lines. The final spectral resolution is 17\AA and the data cover the $5000 - 10000\text{\AA}$ wavelength range. Redshifts were then measured by hand for each object using a standard set of emission and absorption lines for galaxies and AGN.

Eleven sources show clear emission-line spectra (Fig 2, with redshifts ranging from 0.214 to 1.675 (Table 5). At least one of these (A20) can be clearly identified as a narrow-line (ie Seyfert-II-like) AGN. A further two sources (A5 and A25) show a stellar spectrum, and are not considered in this paper further. We did not obtain any clear redshift identification for the two remaining sources, A15 (Fig 3) and A18. We do, however, detect the [OII] emission line in the spectrum of A18 at the spectroscopically-confirmed redshift of $z = 1.467$ from Cowie et al (2001). The equivalent widths of the principal emission lines are tabulated in Table 4, as well as the velocity width of the MgII λ 2798 emission line. In most cases the MgII line is comparatively narrow, although we note that there is evidence for a broad component in both A16 and A19.

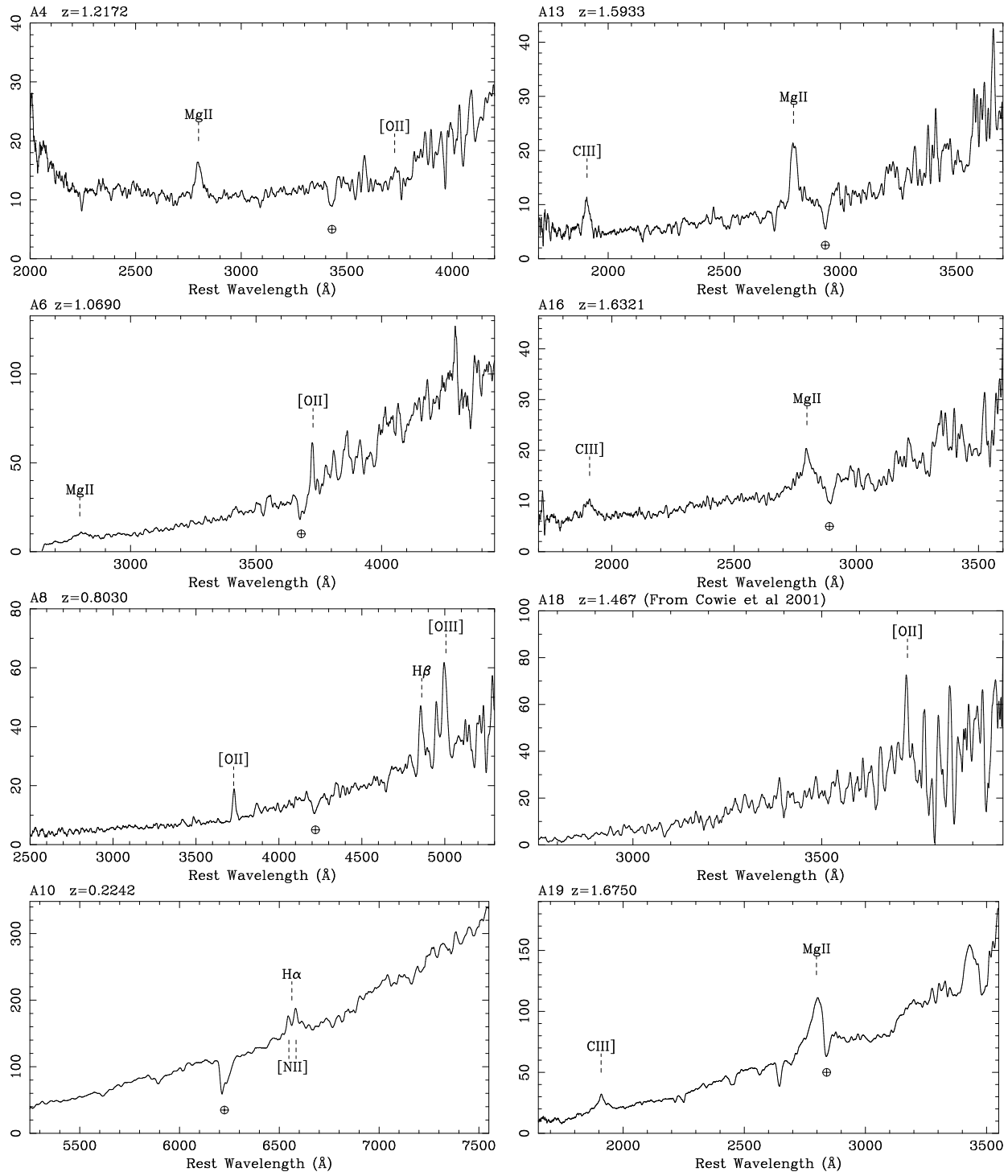


Figure 2. The Keck spectra of the serendipitous sources in the field of A 2390. The spectra are not flux-calibrated, and have been smoothed by 20Å. The \oplus symbol in each spectrum marks the prominent atmospheric absorption feature at around 7600Å.

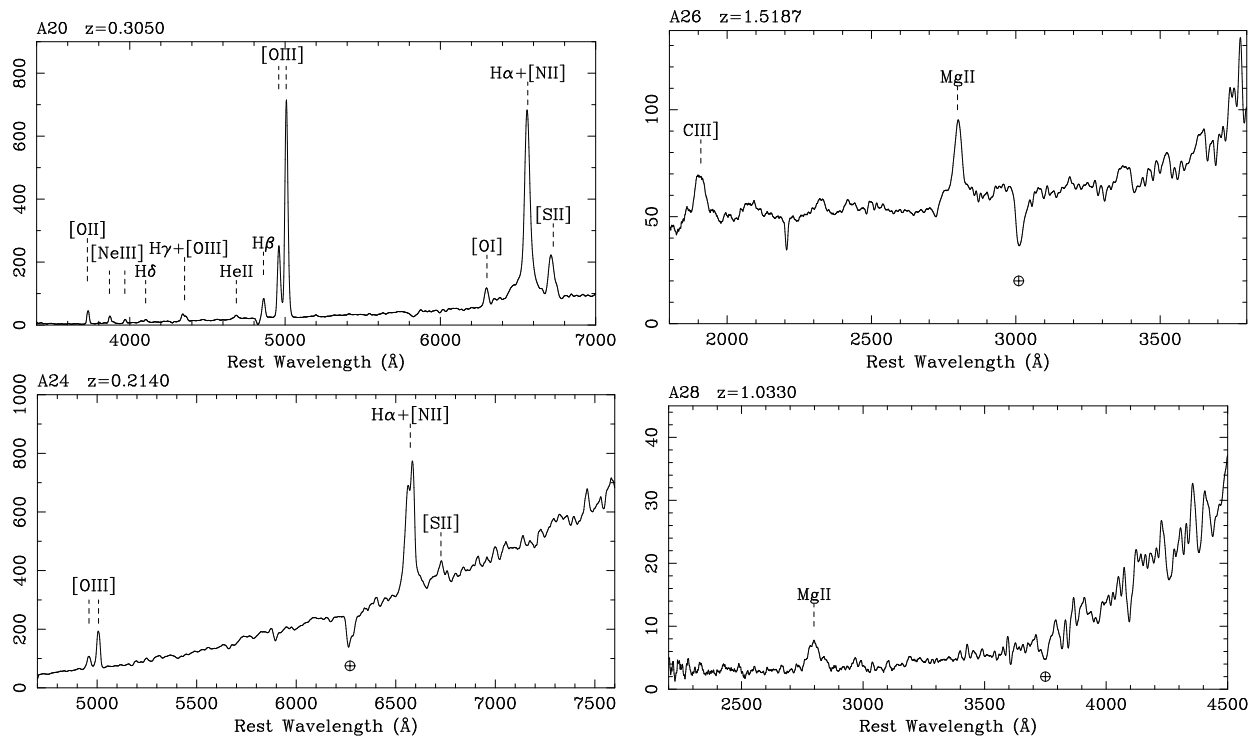


Figure 2. The Keck spectra of the serendipitous sources in the field of A 2390 (ctd).

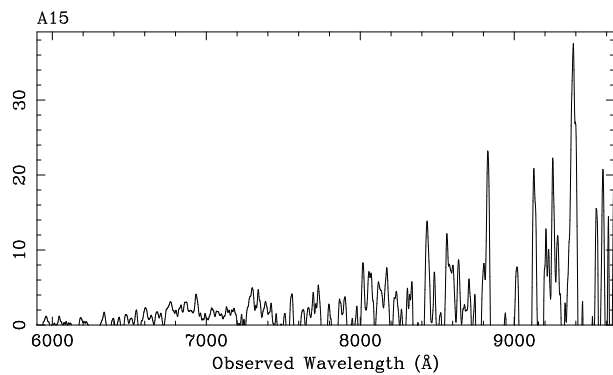


Figure 3. The Keck spectrum of the serendipitous source A15.

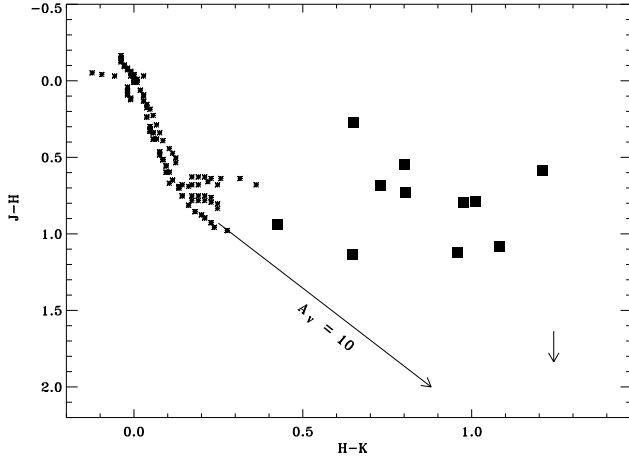


Figure 4. The near-infrared colour-colour plot for the A 2390 background sources (filled squares). The star symbols show the infrared colours of main sequence, giant and supergiant stars of all spectral types. The upper limit is that of A15, in which the large $J-H$ break places the object at $z_{\text{phot}} = 2.78$.

2.4 Photometric Redshifts

As it is clear from the near-infrared colours (Fig 4) that we are not observing stellar objects, we use HYPERZ, a publicly available code (Bolzonella, Miralles & Pello 2000) to estimate redshifts for the sources for which we have near-infrared magnitudes. HYPERZ matches template spectra to the observed spectral energy distribution (SED), which is input as the observed magnitudes and their errors in as many bands as possible. The template spectra are convolved with the filter response in each of the input bands. The filter response includes the quantum efficiency of the CCD – particularly important in the I -band where the response of the CCD falls rapidly toward longer wavelengths around 9000\AA . The infra-red filter responses were also folded with the atmospheric transmission at Mauna Kea, which is affected strongly by water vapour absorption features.

The redshift, age and internal reddening of the templates are varied in order to obtain the maximum likelihood χ^2 solution. The template spectra chosen comprised Bruzual & Charlot (1993) synthetic spectra – with a Solar metallicity and a Miller-Scalo initial mass function – and empirical SEDs observed by Coleman, Wu & Weedman (1980), hereafter referred to as CWW. Both sets of templates range from a single burst of star-formation (SF) through ellipticals and spirals (with exponentially decaying SF rates) to a model for continuous SF in an irregular galaxy. The classification of the CWW spectra is based on the observed morphology of the objects, while the Bruzual & Charlot model galaxy type is set according to the star-formation timescale. In addition, since standard models for the synthesis of the hard X-ray background (Setti & Woltjer 1989; Wilman & Fabian 1999; Wilman, Fabian & Nulsen 2000) predict some of our sources to be heavily obscured AGN, we also created a set of template galaxies with obscured AGN components. A standard broken power-law AGN continuum (Granato, Danese & Franceschini 1997) was assumed over the near-infrared/optical range and reddened with dust using the radiation transfer code DUSTY (Ivezić, Nenkova & Elitzur 1999). Since nothing is known about the dust around these sources without any (a priori) redshift information (except that the dust is probably hot to hundreds of degrees Kelvin; see Wilman, Fabian & Gandhi

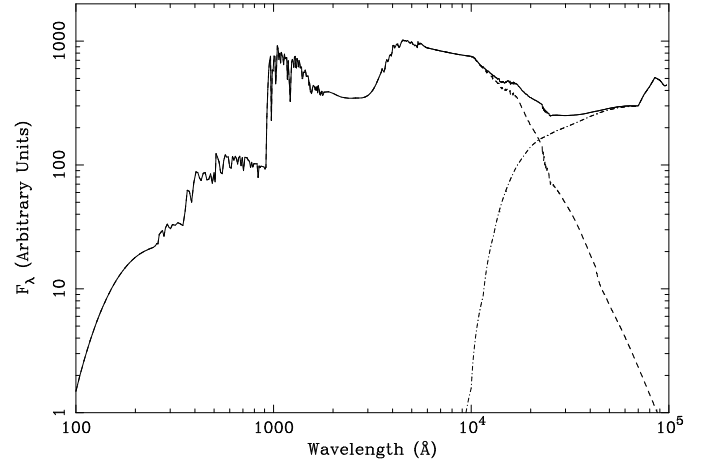


Figure 5. The combined spectrum (solid line) of the CWW Scd template (dashed) with an AGN component (dash-dot) reddened by DUSTY and normalised to have 50% of the total flux at $2.2\mu\text{m}$.

2000; hereafter WFG), a number of models were constructed by varying the dust temperature, composition, optical depth and normalization of the AGN-SED to host-galaxy-SED. The reddened AGN component was added to each of the CWW spectra; one example of this is shown in Fig 5, for the Scd CWW template. With the typical dust properties and composition found in WFG, all the optical light is assumed to be depleted and to emerge preferentially in the mid-infrared regime, with some contribution in the near-infrared. Therefore, the major contribution of the reddened AGN is to the total K -band light.

HYPERZ has a number of options to account for undetected objects, and we adopted the recommended procedure for medium-deep surveys such as ours. We set the flux of a non-detected object and its $1-\sigma$ error equal to $F_{\text{lim}}/2$ in a filter, where F_{lim} is the flux corresponding to the limiting magnitude in that band.

The Galactic column density of $6.81 \times 10^{20} \text{ cm}^{-2}$ in the direction of this cluster corresponds to a reddening $E(B - V) = 0.12$. HYPERZ de-reddens the observed fluxes according to the Galactic reddening law of Allen (1976). Any reddening internal to the galaxy itself was assumed to follow the Calzetti reddening law (Calzetti et al 2000), with a fitting range of A_V between 0.0 and 3.0, in steps of 0.3. The redshift range considered for most objects was 0.0 to 6.0 in steps of 0.05. A maximum absolute Vega magnitude of -25.0 in the B -band (Bessell filter) for a $H_0 = 50$; $q_0 = 0.5$ cosmology was assumed. The results of the photometric-redshift-fitting procedure are shown in Table 5, with examples of the best-fit SED for A18 shown in Fig 6 and for A15 in Fig 7. Fig 7 also shows the contours of confidence for variation of the age of the template galaxy and the amount of reddening required, demonstrating the need for reddening for a range of feasible host galaxy ages in this source.

The photometric redshift estimate agrees well with the spectroscopic measurement (from this paper and from Cowie et al 2001: see Table 5 and Fig 8) for five of our sources: A8, A18, A20, A24 and A28. In addition, our redshift estimate for A15 agrees well with the estimate from Cowie et al (2001), and the spectroscopic redshift for A16 is encompassed within the 90% confidence interval of the photometric-redshift fit. We emphasize that these results were not manipulated to match the spectroscopic redshifts, but constructed as a ‘blind’ test of the photometric redshift fitting procedure. We

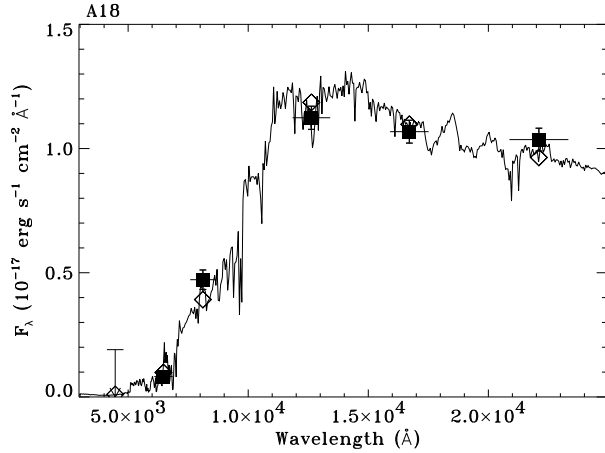


Figure 6. The best-fit spectrum (solid line) for A18 compared to the optical and near-infrared fluxes (solid square markers and B -band limit). The galaxy SED is a single Bruzual & Charlot stellar burst model at $z_{\text{phot}} = 1.45$, close to $z_{\text{spec}} = 1.467$. The x -errorbars are the bandwidths of the filters calculated by HYPERZ according to a Gaussian approximation, and the open diamond markers show the integrated fluxes of the template SED through the individual filters.

have a further three sources (A12, A14 and A27) for which we obtain a photometric redshift without spectroscopic confirmation.

A12 was observed during partial cirrus coverage, which leads to a systematic photometric uncertainty of about 10 per cent in flux when calibrated against the standard star observed nearest in time, as opposed to calibration against all stars observed through the night. Though this in itself is not a significant uncertainty, it creates a degeneracy in the photometric redshift estimate for this source, with the primary solution $z_{\text{phot}} = 2.28$ and the secondary solution $z_{\text{phot}} = 0.66$ being almost equally likely, depending on the calibration. This is because there is no I -band magnitude available, and we only have relatively-shallow DSS limits in the B and the R bands, thus reducing the constraints on this object. I -band photometry would be a strong constraint to resolve the issue. Wherever quoted in this paper, the primary solution stated in Table 5 has been assumed.

2.4.1 A15 at $z \sim 2.8$

The high redshift of $z \sim 2.8$ (with a range of $2.1 < z < 3.3$) predicted for A15 is not surprising, given its large $J - H$ colour (Fig 4). For most of this redshift range ($z > 2.4$) we note that the only major spectral feature we could expect to fall into our observed optical waveband would be the CIII] line, perhaps partway explaining our lack of spectroscopic redshift for this object. This object lies closest to the central cD galaxy and is strongly lensed by a factor of 7.8 (Cowie et al. 2001). This is also detected in a very-deep ISOCAM exposure (Altieri et al. 1999) and the fluxes are reported in Lémonon et al. (1998). WFG used this detection, in conjunction with a SCUBA upper-limit (Fabian et al. 2000) to model the mid-infrared part of the spectrum as due to radiation absorbed in the optical-ultraviolet regime and re-emitted at longer wavelengths. This was done using DUSTY (Ivezić, Nenkova & Elitzur 1999) and is shown as the solid line in the mid- to far-infrared region of Fig 9. Given a central source emitting power-law radiation (for example), and the density, composition, amount and optical depth of surrounding dust, DUSTY calculates a scaled radiative-transfer solu-

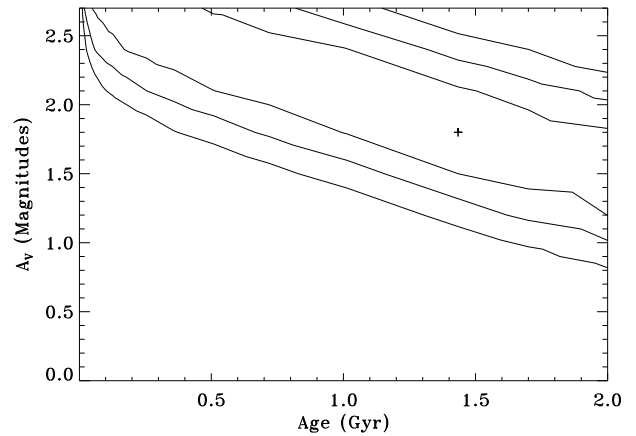
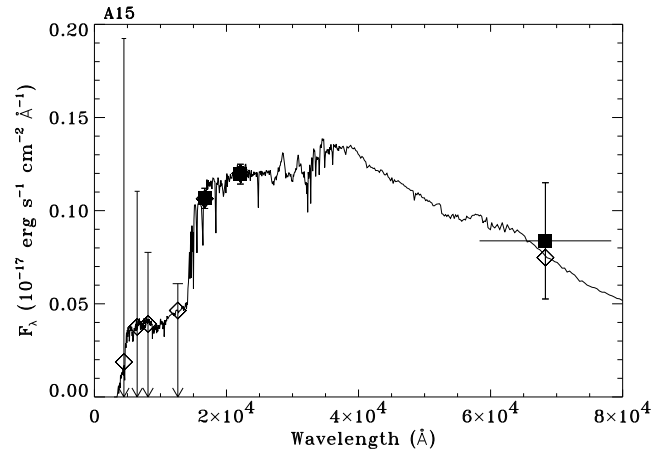


Figure 7. (Top) The most-likely HYPERZ SED for A15 compared to the data, based on limits in B , R , I and J bands and detections in H , K and at $6.7\text{-}\mu\text{m}$. The diamonds show the integrated fluxes of the template SED through the individual filters.

(Bottom) Contours of confidence between the age of the elliptical host galaxy model at $z = 2.78$ and the amount of intrinsic reddening required. The cross indicates the best model, while the confidence intervals are at probabilities of 68%, 95% and 99%. This illustrates the need for reddening in this object, for all host galaxy ages up to 2-Gyr.

tion for different dust temperatures. This spectrum in Fig 9 has been redshifted to $z \sim 2.8$ (as obtained by HYPERZ for the optical-to-near-infrared part of the spectrum) and has been normalised to the $15\text{-}\mu\text{m}$ flux. Both the near-infrared and the mid-infrared parts of the total SED are consistent with the $6.7\text{-}\mu\text{m}$ flux. This model has a dust-temperature of 1500 K at the inner-dust radius, and an optical-depth of 40 at $0.3\text{-}\mu\text{m}$. Though lower temperature models were formally acceptable, these underestimate the SCUBA limit by only a factor of a few. Given that most of the Chandra sources are undetected at sub-millimeter wavelengths (e.g. Fabian et al. 2000), the $850\text{-}\mu\text{m}$ flux is likely to lie well below the SCUBA limit. Reducing the temperature significantly begins to cut into the $850\text{-}\mu\text{m}$ flux and also miss the $6.7\text{-}\mu\text{m}$ flux completely. (See WFG for more details. Note that although the redshift presented therein has since changed, this only makes the conclusion of hot dust even more robust.) A18 was also detected by ISOCAM (Altieri et al 1999). We do not produce an SED here since no mid-infrared fluxes have been published.

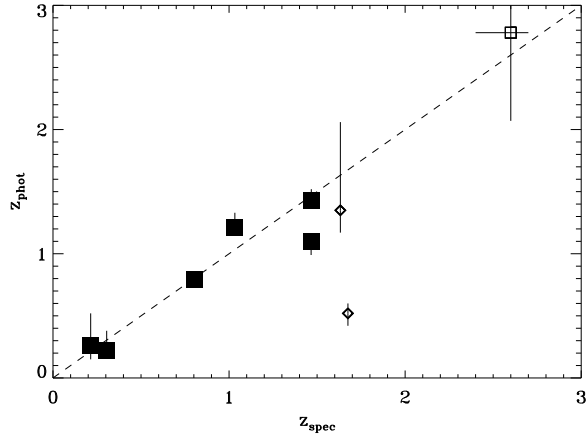


Figure 8. Comparison of spectroscopic and photometric redshifts for nine sources. The y -errorbars are taken from the 90% confidence limits given by HYPERZ. For the object A15 at $z_{\text{phot}} = 2.78$, the value of $z_{\text{spec}} = 2.6$ quoted for comparison is the photometric-redshift obtained by Cowie et al (2001). The two objects marked by unfilled diamonds (A16 and A19) show other indications of having their light dominated by relatively unobscured quasars, and are discussed further in the text.

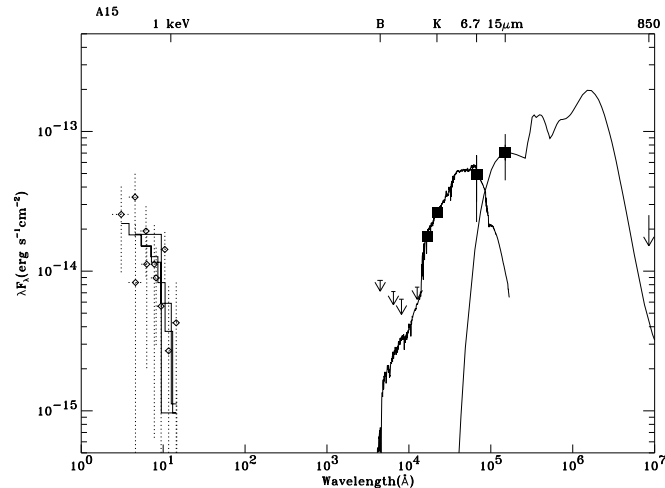


Figure 9. The total spectral energy distribution for A15. The X-ray data are marked by open diamond markers with error bars. Our optical and near-infrared values and limits are marked as solid squares. The best-fit model to the X-ray spectrum (see Table 6) is shown as a solid line, and the other solid lines show the fits obtained in HYPERZ (optical to near-infrared) and DUSTY (normalized to the 15- μm flux; see text for details). The *SCUBA* upper-limit is shown as the arrow at 850- μm .

2.4.2 Problem sources

Our photometric redshift estimates do not agree so well with the spectroscopic redshifts of A16 and A17, and the estimate is particularly bad for A19; in all three cases the secondary solution to the photometric redshift is no better. A16 is the closest match of these three sources, with the 90% confidence interval of the photometric-redshift-fitting encompassing the spectroscopic measurement.

Part of the redshift mismatch for A17 is due to its proximity to a bright neighbour about 3 arcsec to the south-east (Fig 10). A small aperture (2.7 arcsec diameter) was used to extract the flux, but the source is not well resolved from its neighbour in the *B*-

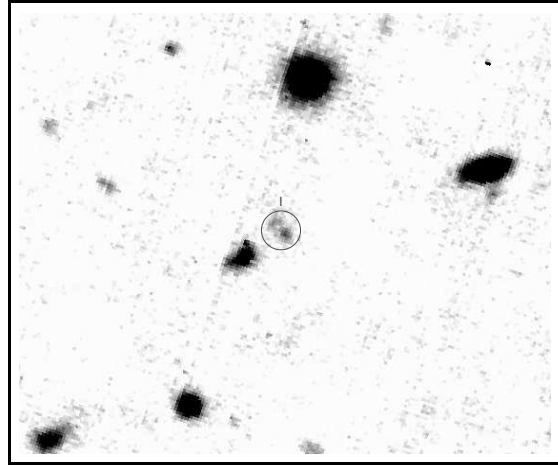


Figure 10. *CFHT* *I*-band image of A17 showing a double structure. In addition there is confusion with the neighbour to the south-east in the *B* and the *R*-band images, where the seeing is much worse. The image side is 30-arcsec long and North is to the top, East to the left.

and *R*-band data due to the very poor seeing at the time of the observations. Thus the *B*- and *R*-band magnitudes may be inaccurate due to contamination from the neighbour and loss of source flux outside the small aperture. The source and its neighbour are well resolved in both the UKIRT and *CFHT* observations; in addition, the *I*- and *H*-band images show the source itself to have a second component ~ 1 arcsec to the NE (Fig 10). This second component is probably too faint to be a serious source of contamination to the observed magnitudes. We speculate that the small NE component could be an extended (~ 8 kpc from the source) cloud of emission-line gas associated with the source. If it were at the same redshift as the source of z_{phot} , then strong line emission from [OII] and [NII] and/or $\text{H}\alpha$ could account for this feature showing up only in the *I*- and *H*-bands. We note, though, that the *on-source* spectrum of Cowie et al (2001) – which may well not include this NE component – does not show strong [OII], and any [OIII] line emission from this would emerge in the *J*-band.

A19 appears point-like in the near-infrared images, with a full-width-half-maximum close to the seeing values, and is easily resolved from any neighbouring sources. Its brightness at optical wavelengths implies that there are no obvious breaks in the broadband spectrum (see Fig 11) to anchor the photometric redshift fitting. Moreover, the lack of an archival *I*-band image for this object reduces the constraints available for the fitting. A19 is one of two objects with evidence of a broad MgII emission line component in its optical spectrum (Table 4). The X-ray spectrum is, however, fit with a power-law model and excess absorption (see section 2.5). Combined with its high *B*-band magnitude and stellar spatial profile, we are most likely viewing the ‘naked’ quasar in this object. (The only other object showing a similar broad component to the MgII emission line is A16, which also has little X-ray absorption.)

The observed broadband spectrum shown in Figure 11 is also consistent with a very young early type system before the Balmer break sets in. In fact, the best photometric-redshift fit to the A19 magnitudes using galaxy templates, and restricting the fits to M_B fainter than -25 gives such a young (0.26 Gyr) early-type system, but at a redshift of $z_{\text{phot}} = 0.52$, different to z_{spec} . A broken power-law continuum template (due to Granato, Danese & Franceschini 1997) gave a fit at $z_{\text{phot}} = 2.36$ with a significantly worse $\chi^2_{\text{reduced}} = 9$, while a free fit with a high signal-to-noise empirical

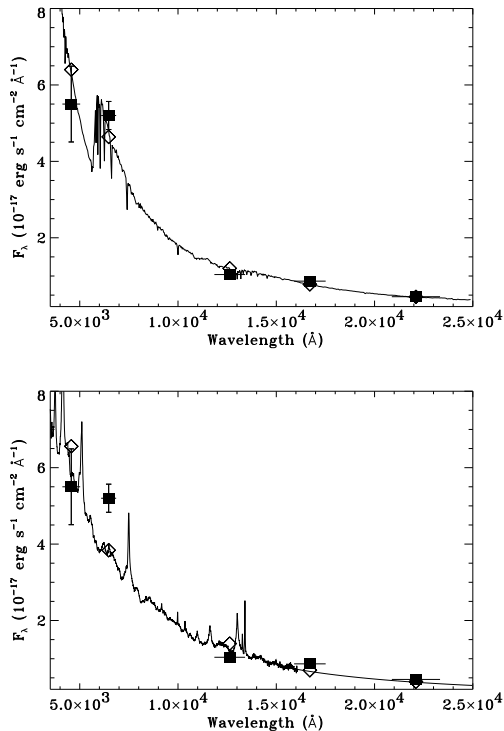


Figure 11. The best-fit SED to A19 using all templates gives a young (260-Myr-old) system at $z_{\text{phot}} = 0.52$ (top), while an empirical QSO template fixed at $z = z_{\text{spec}}$ and a small $A_V = 0.2$ has a similar slope to the observed fluxes, with some deviation in the *R*-band.

QSO spectrum (from Francis et al. 1991) gives $z_{\text{phot}} = 0.32$. All the fits are far from the inferred z_{spec} . This is primarily because the photometric-redshift fitting technique relies on breaks in the broadband spectrum, which this object does not possess. We do not think that the discrepancy in redshifts could be due to contamination by strong line emission. To demonstrate this, we fit the magnitudes by the empirical unobscured QSO spectrum of Francis et al (1991), but now with its redshift fixed at $z = z_{\text{spec}} = 1.675$. The fit is plausibly acceptable (Fig 11), except where it falls well below the observed flux in the *R*-band. However, there are no obvious emission lines between MgII and CIII] that could be boosting the *R* magnitude.

Finally, we also attempted to fit the colours and magnitudes of A19 by combined quasar+host galaxy spectra, quantifying the amount of dilution by comparing the equivalent width (EW) of the observed emission lines (e.g. EW(MgII in A19)= 34Å) to the EW found by Francis et al. (1991) for an average unobscured quasar spectrum (50Å for MgII). This decrement can be interpreted as an increment in the continuum due to the host galaxy contribution. An SED was constructed with a typical AGN-power law contribution at 34/50 that of the total continuum at 2797Å, the rest-wavelength of MgII. Four different SEDs were constructed with the four CWW host galaxies models. However, the best-fit to A19 was a powerlaw-plus-continuous-star-formation model at $z_{\text{phot}}=0.06$ and $\chi^2_{\text{reduced}} = 10$, again far from z_{spec} . We also tried a reddened-AGN-spectrum-plus-galaxy spectrum, but again obtained the wrong redshift. Thus we infer that if the photometry and optical-line identifications are correct, the template of this galaxy does not exist within our library, although the MgII broad

line most likely indicates a relatively-unobscured quasar. *I*-band photometry would be a first-step to constrain this object more. We note that A19 appears to fit into the class of objects identified by Maiolino et al (2001) which have blue optical colours, and moderate X-ray absorption. The reduced absorption due to dust compared to that expected from the gas column density suggests that such AGN have dust-to-gas ratios very different to Galactic values. If this is the case for A19, then it is not surprising that HYPERZ has difficulty in finding a solution.

A16, the third object with a slight redshift mismatch, is similar to A19. As already mentioned these are the two sources with good fits to broad MgII λ 2798 components. There is no break in the broad-band optical/near-infrared SED of either, with flux-per-unit-wavelength increasing monotonically towards the optical. A16 is, in fact, best fit with a naked QSO spectrum at a redshift of 1.35, with the spectroscopic redshift of 1.6321 being encompassed within the 90% confidence interval of the HYPERZ fit. This is consistent with the X-ray spectral analysis for this object, which reveals little absorption (Table 6). Curiously, A16 and A19 are also located close together on the sky, with a separation of just over an arc-minute between them.

2.5 X-ray spectra

We attempted to extract and model the X-ray spectrum of those serendipitous sources for which a redshift (either spectroscopic or a photometric estimate) was available. The fitting was performed in XSPEC (Arnaud 1996). In practice, we can extract a usable spectrum only for the brighter sources (A6, A15, A16, A18, A19, A20, A24 and A26). We were not able to fit A28, but note that most of the counts lie between 0.7 and 0.8 keV. We fit the model to the data only between 0.3 – 0.7 keV, and the spectra were grouped to have a minimum of 20 counts in each bin. In all cases we assumed the source to have a power-law spectrum with possible intrinsic absorption, ie in excess of the Galactic column density. In all cases we let both the power law slope (Γ) and the excess N_{H} vary freely; if this fit required a value of Γ that was appreciably different from the canonical value of $\Gamma = 2$, we repeated the fit with Γ fixed at 2. Unless otherwise noted in Table 6, the data from both observations were fit simultaneously. We present the results in Table 6. Although A8 had too few counts to fit the spectra properly, we can at least say that the spectra appear to be consistent with no intrinsic absorption, for a power-law model with $\Gamma = 2$ fixed.

The best fits to the spectra of A18, A19 and A20 are shown in Fig 12, demonstrating that A18 and A20 require substantial amounts of excess absorption, whereas A19 does not. The contours of confidence for the values of freely fitting parameters N_{H} and Γ in the fits to A15, A18, A19 and A20 spectra are shown in Fig 13. These show that the conclusion of excess absorption is robust for A18, A19 and A20 (although less so for A15) for all reasonable values of Γ . Note that the intrinsic absorption N_{H} inferred from the X-ray spectra is in all cases more than that implied by the moderate amounts of reddening A_V (Table 5) found from the photometric redshift fitting in the previous section. However, any reddening of the host galaxy is due to dust within the galaxy, whereas the line of sight to an active nucleus is expected to pass through additional absorption much closer in to the central engine. As discussed in the previous section, one source, A19, shows evidence for a dust-to-gas ratio other than Galactic.

It is also possible to examine the faint sources which do not have enough counts to justify spectral fitting. We used XSPEC to predict the soft-to-hard (S/H) ratio that would be observed (on

the I3, S2, S3 and S4 chips) for an absorbed (intrinsic + Galactic) power-law source placed at a range of redshifts with a variety of intrinsic column densities (cf. Table 4 in Crawford et al. 2001. Note that this table assumes zero Galactic absorption). Next, the observed S/H ratios (Table 1) for sources with a redshift determination were compared with the predicted values, from the same chip, in order to constrain the intrinsic column densities. These are listed in Table 7. Predictions were made for powerlaw-indices Γ of 1.4 and 2. Note that the maximum observable S/H ratio for a fixed photon-index will be from an intrinsically-unabsorbed source. Any non-zero intrinsic absorption could only deplete the soft counts and decrease the S/H ratio. This is basis of the predictions of larger Γ in the last column of Table 7 for the very soft sources (with observed S/H greater than the predicted maximum for $\Gamma = 2$ and for $\Gamma = 1.4$). It is not possible to constrain the intrinsic absorption in these cases, since larger photon-indices could also imply larger column densities.

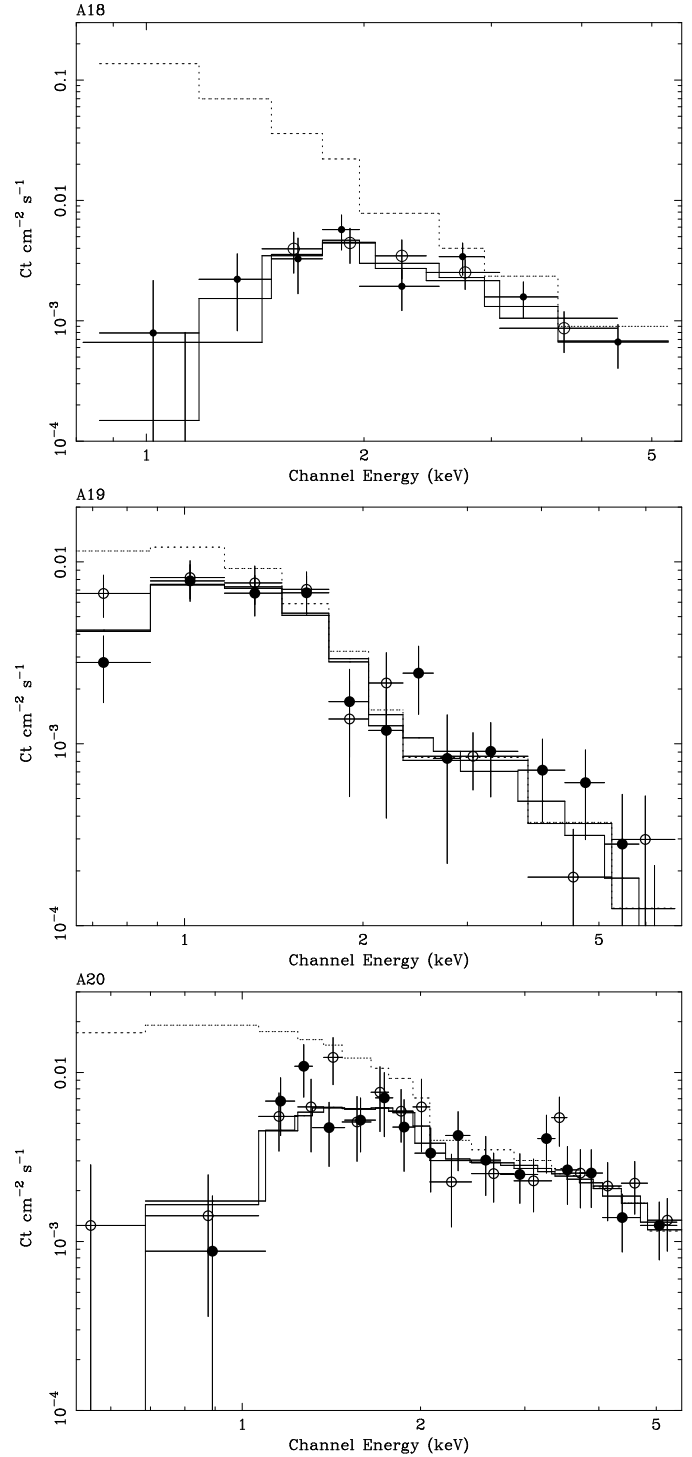


Figure 12. The X-ray spectra of A18, A19 and A20, showing the best-fit absorbed power law models to the data (solid line), and the fit but now without the intrinsic absorption (dotted line). The parameters of these best-fit models are given in Table 6. The solid and open circle markers indicate the spectrum extracted for the source from the two different datasets.

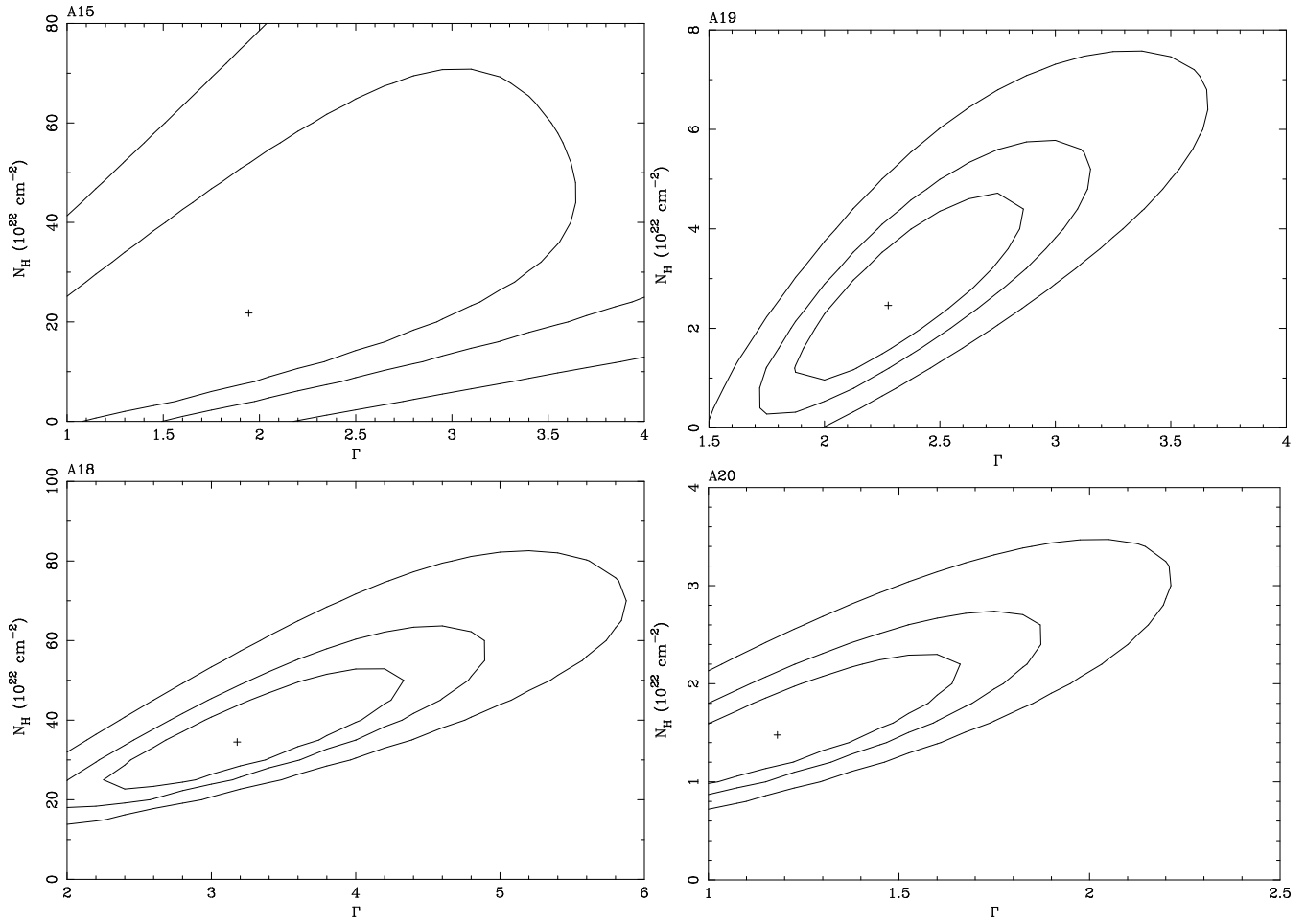


Figure 13. The confidence contours on the parameters Γ and intrinsic absorption N_H for the X-ray spectral fits to A15, A18, A19 and A20.

3 SUMMARY OF RESULTS AND DISCUSSION

We have detected 31 serendipitous sources in the field of A 2390. The majority of these (18 in total) were detected on the ACIS-S3 chip, which contains the pointing target of the observations, A 2390. We do not consider that our results are enhanced by weak gravitational lensing by the cluster. The degradation of the PSF and vignetting make the other chips less sensitive to faint sources. Only three of the sources are sufficiently close to the line of sight through the centre of the cluster potential to be significantly magnified by gravitational lensing. These are A15, A17 and A18, which are magnified by 7.8, 2.8 and 2.1 respectively (Cowie et al 2001). None of the sources appears significantly more extended than the PSF expected at that position on the detectors, and are hence all consistent with being point sources. About 50 per cent of the sample have soft X-ray spectra ($S/H > 3$), and about one-third of the sources show hard spectra (ie $S/H < 2$). The six sources with the hardest colours ($S/H < 1.5$) are A2, A15, A18, A20, A24 and A30. Eight of the sources showed evidence for variability on an eleven-month timescale.

We have fitted an absorbed power-law model to simple X-ray spectra of the eight sources with sufficient counts and a known redshift. The unabsorbed (de-magnified) 2–10 keV luminosity ranges from 0.1 to $30 \times 10^{44} \text{ erg s}^{-1}$. The intrinsic absorption required varies from none (in two cases) to $35 \times 10^{22} \text{ cm}^{-2}$. Most of these sources are thus in the Compton-thin regime. We note that the two sources for which the X-ray spectrum indicates the most intrinsic absorption ($N_{\text{H}} > 10^{23} \text{ cm}^{-2}$) are those – A15 and A18 – that are magnified from gravitational lensing by the foreground cluster A 2390. Without the presence of the foreground cluster we would not have been able to observe these sources so clearly. We have found no sources in this field which are clearly Compton-thick (i.e. have an absorbing column $> 10^{24} \text{ cm}^{-2}$). The lack of such sources is, however, consistent with predictions of the observable density of Compton-thick objects at this flux level (Wilman & Fabian 1999). As well as its high intrinsic column, A18 also has an intrinsic luminosity of $> 10^{45} \text{ erg s}^{-1}$ (correcting for the gravitational lensing magnification); thus it is a good candidate for an X-ray Type II quasar.

We have clear optical identifications for 23 of the sources, and imaged twelve in the near-IR, choosing preferentially the optically-faint harder ones. All the sources were detected in *J*, *H* and *K*, including one source (A15) that was not detected down to faint optical levels. Optical spectra were taken for fifteen of the sources (including two objects which had stellar spectra; note also that the magnitudes of A9 and its stellar profile in the DSS strongly suggest that this source is also a star). We have obtained a new spectroscopic redshift for 10 sources (3 others were already in the literature), and estimated a photometric redshift for a further four sources (one of which is in agreement with a previously published photometric estimate). We tested the results of photometric redshift fitting for those sources for which we also had optical spectra, and found reasonably good agreement. We show the redshift distribution for all the sources in Fig 14. The four very hard X-ray sources for which we have redshifts span the whole redshift range observed, at 0.214, 0.305, 1.467 and 2.78. The remainder of the optical spectra showing emission lines are of softer sources. We have photometric redshifts for a further 3 hard sources.

The *K* magnitude and the redshift z for all of our sources follow the relationship known for radio galaxies (Fig 16; Eales et al 1993), even though none of our serendipitous sources are coincident with radio detections listed in the NASA/IPAC Extragalactic

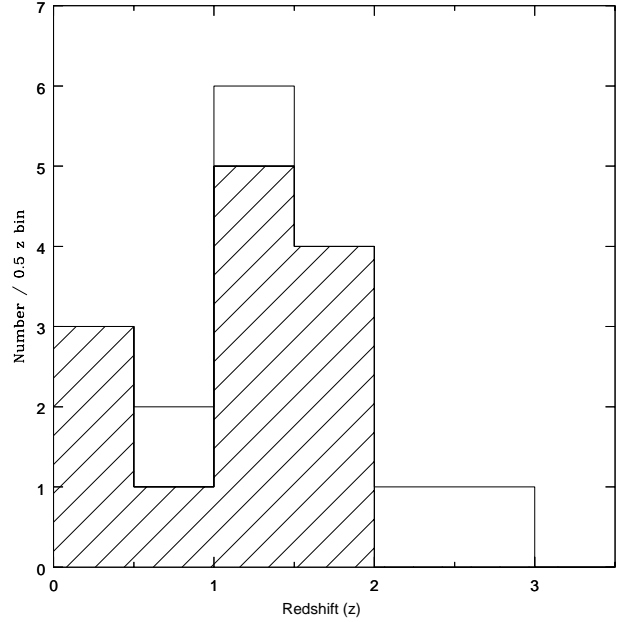


Figure 14. The redshift distribution, where known, of the serendipitous sources in the field of A 2390. The shaded boxes indicate those sources that have a spectroscopic redshift rather than a photometric redshift.

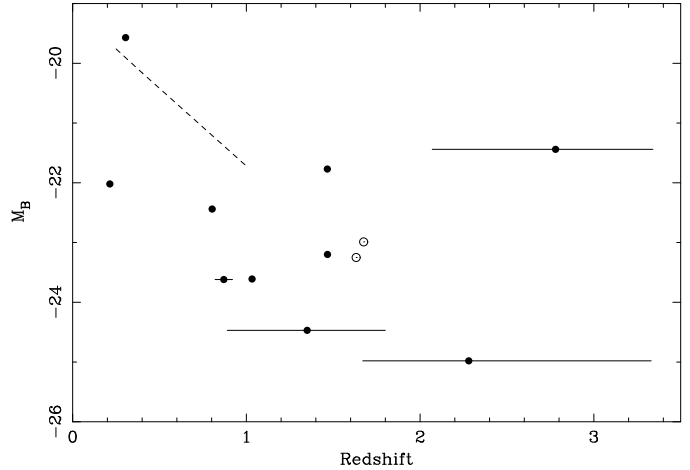


Figure 15. The absolute M_B of the host galaxies from the HYPERZ fitting plotted against redshift. The dashed line shows the magnitude-redshift relation of blue field galaxies out to $z \sim 1$ from Lilly et al (1995). A16 and A19 are marked by open circle symbols, as their light is thought to be dominated by a quasar component.

Database (NED; this area of sky is not covered by the FIRST catalogue). This results contrasts with the tendency for the *Chandra* sources found in the ELIAS survey area to lie well above the *K* – z relation (Willott et al 2001). The *B* magnitude of the host galaxies inferred from the photometric redshift fitting increases with redshift (Fig 15). Comparison of our magnitudes to the the magnitude-redshift distribution of the blue field galaxy out to $z \sim 1$ (from Lilly et al 1995), indicates that the majority of our sources lie in brighter, and presumably more massive galaxies than the general field population.

All the sources (except for A15) with spectroscopic redshifts

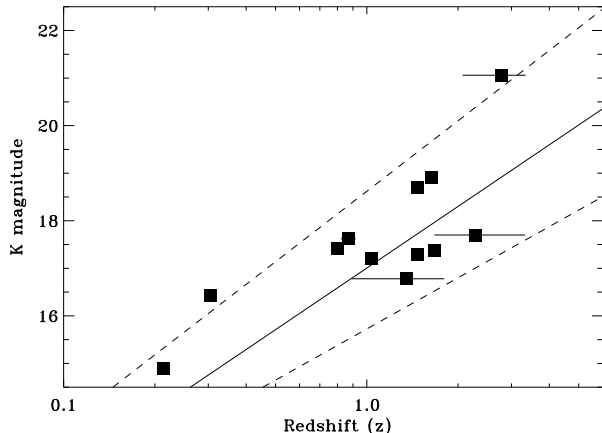


Figure 16. The K - z relation for our sources. The solid line shows the K - z relation for radio galaxies, and the dotted lines indicate the scatter of the radio galaxies about this line (taken from Eales et al 1993). The K -magnitudes of A15, A17 and A18 have been corrected for the magnification due to gravitational lensing.

show optical emission-line spectra, indicative (in combination with their point-source appearance in the optical/near-IR bands and the large fraction showing X-ray variability) of AGN-type behaviour. Seven of the nine sources at high enough redshift (and with optical spectra) show the MgII emission line. We note that A18 – one of the two sources with large amounts of intrinsic absorption – shows no sign of MgII emission (although its expected position is right on the edge of the observed spectrum). The other heavily absorbed source, A15, shows no sign of CIII] λ 1909, which should be observed at $\sim 7180\text{\AA}$ if the source is at the photometric estimated redshift of 2.78 (Fig 3). We do not have an X-ray spectrum for the other source that does not show MgII emission (A8), although we note that it is a soft X-ray source (Table 1). There does not seem to be a broad component to the Balmer emission lines in A20 or in A24, which are two X-ray-hard sources, at least one of these being a narrow-line Seyfert.

Though we do not have enough sources for clustering statistics, we note that at least two sources (A17 and A18) lie at the same redshift, with a separation of about 40 arcsec. Two other sources (A16 and A19) – both showing evidence of harbouring relatively-unobscured AGN – are also separated by about an arcmin, at redshifts of 1.632 and 1.675 respectively.

4 CONCLUSIONS

Optical and near-infrared follow-up work on two ~ 10 ks *Chandra* exposures of the A 2390 field resulted in 23 out of 31 detected sources being identified. The 0.5–7 keV fluxes of these sources range from just below, to a few times, $10^{-14} \text{ erg cm}^{-2} \text{ s}^{-1}$. Two of the sources are stars and 13 have optical emission-line spectroscopic redshifts ranging from 0.2–1.7. One source, A10 at $z = 0.2242$, probably lies within the cluster A 2390. Apart from the two lowest redshift non-cluster objects, the rest with optical emission lines have soft X-ray spectra. We have JHK photometry of 12 sources which enabled us to obtain photometric redshifts for a further 4 sources. We find good agreement between photometric and spectroscopic redshifts where both are available. Of the 12 sources without either optical spectroscopy or near-infrared imaging, about

half are probably hard ($S/H < 2$). 4 of this hard group are undetectable on the DSS and 4 have no identification.

We have obtained an insight into the properties of the harder, fainter population from the 3 gravitationally-lensed sources (A15, A17 and A18). All would have been detected in X-rays without the lensing, A15 and A17 would have been just detected and A18 well detected. A15 and A18 have hard X-ray spectra. The magnification has made the near-infrared work easier and Cowie et al (2001) have obtained (similar) infrared spectroscopic redshifts ($z = 1.47$) for both A17 and A18 and a photometric redshift ($z \sim 2.6$ confirmed here) for A15. A15 and A18 appear to be genuine obscured quasars with intrinsic 2–10 keV luminosities of $2 \times 10^{44} \text{ erg s}^{-1}$ and $2 \times 10^{45} \text{ erg s}^{-1}$ respectively. They were both also detected in the mid-infrared by ISO. Model spectral energy distributions for the $z \sim 2.6$ source indicate that the reprocessed radiation is emitted by hot (1500 K) or warm dust, peaking at 100–200 μm .

The results of our modest sample are consistent with, and extend, previous work on deeper fields (e.g. Barger et al 2001). We find that i) most of the sources at 0.5–7 keV fluxes around $10^{-14} \text{ erg cm}^{-2} \text{ s}^{-1}$ can be optically identified, although deep optical and infrared imaging is required; ii) about one half of the sources, mostly the X-ray softer ones, have optical emission lines with which spectroscopic redshifts can be obtained; iii) photometric redshifts work well and enable some more redshifts to be obtained, particularly of harder sources; iv) about one third of the sources are both optically faint and hard. These last sources are likely to be important for producing the harder parts of the XRB, which peaks in νI_ν at $\sim 30 \text{ keV}$, although the class of faint Compton-thick sources which should dominate at the peak may not yet have been detected. If A15 is typical of the optically-faint hard sources, then they are obscured quasars in early-type bulges at redshifts of 2–3, or possibly higher. The absorbed X-ray and UV emission emerges in the mid-infrared.

5 ACKNOWLEDGEMENTS

We are grateful to the *Chandra* project for the X-ray data, and to M. Bolzonella J.-M. Miralles and R. Pello for making HYPERZ available. We thank Stefano Ettori for the use of his software in reducing the X-ray data, and Andrew Firth for his help with HYPERZ. CSC and ACF thank the Royal Society, PG thanks the Isaac Newton Trust, the Overseas Research Trust and Fitzwilliam College Trust Fund, and RJW the PPARC for financial support. Support for AJB was provided by NASA through the Hubble Fellowship grant HF-01117.01-A awarded by the Space Telescope Science Institute, which is operated by the Association of Universities for Research in Astronomy, Inc., for NASA under contract NAS 5-26555. AJB and LLC acknowledge support from NSF through grants AST-0084847 and AST-0084816, respectively.

The United Kingdom Infrared Telescope is operated by the Joint Astronomy Centre on behalf of the U.K. Particle Physics and Astronomy Research Council. This research made use of data obtained from the Isaac Newton Group Archive at the UK Astronomy Data Centre, Cambridge, and the Canadian Astronomy Data Center, which is operated by the Dominion Astrophysical Observatory for the National Research Council of Canada’s Herzberg Institute of Astrophysics. This research has also made use of the NASA/IPAC Extragalactic Database (NED), and the Digitized Sky Surveys which were produced at the Space Telescope Science Institute under U.S. Government grant NAG W-2166.

REFERENCES

- Allen D.A., 1976, MNRAS, 174, 29P
- Allen S.W., Etori S., Fabian A.C., 2001, MNRAS accepted (astro-ph-0008517)
- Altieri B., Metcalfe L., Kneib J.P., McBreen B. et al., 1999, A&A, 343, L65
- Arnaud K.A., 1996, "Astronomical Data Analysis Software and Systems V", eds. Jacoby G. and Barnes J., ASP Conf. Series vol. 101, 17
- Barger A.J., Cowie L.L., Mushotzky R.F., Richards E.A., 2001, AJ, 121, 662
- Bolzonella M., Miralles J.-M., Pello R., 2000, A&A, 363, 476.
- Brandt W.N. et al 2001 (astro-ph/0102411)
- Bruzual G.A., Charlot S., 1993, ApJ, 405, 538
- Calzetti D., Armus L., Bohlin R.C., Kinney A.L., Koornneef J., Storchi-Bergmann T., 2000, ApJ, 533, 682
- Coleman G.D., Wu C.-C., Weedman D.W., 1980, ApJS, 43, 393
- Comastri A., Setti G., Zamorani G., Hasinger G., 1995, A&A, 296, 1
- Cowie L.L. et al 2001, ApJ, 551, L9
- Crawford C.S., Fabian A.C., Gandhi P., Wilman R.J., Johnstone R.M., 2001, MNRAS in press
- Eales S.A., Rawling S., Dickinson M., Spinrad H., Hill G.J., Lacy M., 1993, ApJ, 409, 578
- Epps H.W., Miller J.S., 1998, Proc SPIE, 3355,48
- Fabian A.C. et al 2000, MNRAS, 315, L8
- Francis P.J., Hewett P.C., Foltz C.B., Chaffee F.H., Weymann R.J., Morris S.L., 1991, ApJ, 373, 465
- Giacconi R. et al 2001 (astro-ph/0007240)
- Granato G.L., Danese L., Franceschini A., 1997, ApJ, 485, 147
- Hasinger G. et al 1998, A&A, 329, 482
- Hornschemeier A.E. et al 2001 (astro-ph/0101494)
- Ivezić Z., Nenkova M., Elitzur M., 1999 (astro-ph/9910475)
- Lehmann I. et al, 2001 (astro-ph/0103368)
- Lemonon L., Pierre M., Cesarsky C.J., Elbaz D., Pello R., Soucail G., Vigroux L., 1998, A&A, 334, L21
- Lilly S.J., Tresse L., Hammer F., Crampton D., Le Fevre, O., 1995, ApJ, 455, 108
- Madau P., Ghisellini G., Fabian A.C., 1994, MNRAS, 270, L17
- Maiolino R. Marconi A., Salvati M., Risaliti G., Severgnini P., Oliva E., La Franca F., Vanzì L., 2001, A&A, 365, 28
- Mushotzky R.F., Cowie L.L., Barger A. Arnaud K.A., 2000, Nature, 404, 459
- Setti G., Woltjer L., 1989, A&A, 224, L21
- Stark A.A., Gammie C.F., Wilson R.W., Bally J., Linke R.A., Heiles C., Hurwitz M., 1992, ApJS, 79, 77
- Tozzi P. et al 2001 (astro-ph/0103014)
- Willott C.J. et al, 2001 (astro-ph/0105560)
- Wilman R.J., Fabian A.C., 1999, MNRAS, 309, 862
- Wilman R.J., Fabian A.C., Gandhi P., 2000, MNRAS, 318, L11
- Wilman R.J., Fabian A.C., Nulsen P.E.J., 2000, MNRAS, 319, 583
- Yee H.K.C. et al 1991, A&AS, 88, 133

Table 1. Serendipitous X-ray sources in the field of the cluster A2390

Name	Seq. No. [Chip]	RA _X	Δα _X (^h)	DEC _X	Δδ _X (^m)	WAV (cts)	(err)	Sig	0.5-7 keV (cts)	(err)	0.5-2 keV (cts)	(err)	2-7 keV (cts)	(err)	S/H	(err)	PSF ratio
A1	800008 [I2]	21:52:34.92	(1.2)	+17:38:10.0	(1.5)	22.80	(8.83)	7.97	55.76	(8.81)	36.39	(6.77)	18.55	(5.58)	1.96	(0.69)	1.11
A2	800008 [I3]	21:52:44.42	(1.6)	+17:43:54.6	(1.6)	8.01	(4.91)	4.05	15.59	(4.83)	9.37	(3.52)	7.32	(3.48)	1.28	(0.77)	1.02
	800009 [I3]	–	–	–	–	–	–	–	<8.76	–	<6.07	–	<5.93	–	–	–	–
A3	800008 [I3]	–	–	–	–	–	–	–	<5.53	–	<2.94	–	<4.72	–	–	–	–
	800009 [I3]	21:52:55.76	(0.7)	+17:44:33.6	(0.5)	11.17	(3.91)	4.95	12.62	(3.92)	8.33	(3.11)	<4.76	–	>1.74	–	0.56
A4	800008 [I3]	–	–	–	–	–	–	–	<4.63	–	<4.58	–	<0.41	–	–	–	–
	800009 [I3]	21:53:00.91	(0.4)	+17:44:51.9	(0.7)	8.94	(3.42)	4.20	11.46	(3.58)	7.88	(2.90)	<4.18	–	>1.89	–	0.48
A5	800009 [I2]	21:53:04.88	(0.6)	+17:38:33.3	(0.5)	13.04	(4.07)	5.73	15.76	(4.20)	13.54	(3.79)	<3.56	–	>3.80	–	0.82
A6	800008 [S3]	21:53:20.69	(0.1)	+17:41:19.2	(0.1)	40.76	(6.47)	19.22	41.34	(6.48)	29.19	(5.44)	12.18	(3.51)	2.40	(0.82)	1.10
	800009 [S3]	21:53:20.68	(0.1)	+17:41:19.1	(0.1)	57.74	(7.79)	23.77	59.77	(7.79)	50.51	(7.15)	9.23	(3.09)	5.47	(1.99)	1.11
A7	800008 [S3]	21:53:22.54	(0.2)	+17:40:18.2	(0.1)	10.65	(3.35)	5.44	11.04	(3.35)	6.96	(2.67)	4.09	(2.02)	1.70	(1.06)	0.95
A8	800008 [S3] †	21:53:23.78	(0.1)	+17:39:29.8	(0.1)	18.47	(4.40)	9.04	19.74	(4.52)	18.92	(4.40)	<2.04	–	>9.27	–	1.13
	800009 [S3]	21:53:23.82	(0.1)	+17:39:29.8	(0.2)	15.85	(4.06)	7.97	23.25	(4.87)	19.21	(4.42)	<4.08	–	>4.71	–	0.86
A9	800008 [S1] †	21:53:23.81	(0.5)	+17:30:21.5	(0.4)	29.62	(6.42)	9.95	40.96	(6.76)	36.34	(6.25)	<5.18	–	>7.02	–	0.62
A10	800008 [S3]	–	–	–	–	–	–	–	6.53	(3.19)	<5.62	–	<3.02	–	–	–	–
	800009 [S3]	21:53:25.26	(0.3)	+17:43:21.9	(0.2)	11.63	(3.78)	5.30	13.04	(3.79)	13.44	(3.79)	<0.43	–	>31.26	–	1.45
A11	800008 [S2]	21:53:26.40	(0.6)	+17:35:16.8	(0.3)	13.00	(3.88)	6.01	16.54	(4.16)	14.53	(3.87)	<2.98	–	>4.88	–	1.14
A12	800009 [S4]	21:53:29.01	(0.5)	+17:48:54.3	(0.6)	12.02	(4.63)	5.02	18.21	(4.65)	12.28	(3.79)	6.04	(2.69)	2.03	(1.10)	1.13
A13	800009 [S3]	21:53:31.60	(0.3)	+17:47:04.0	(0.3)	18.45	(4.51)	8.41	21.61	(4.75)	18.78	(4.39)	<3.62	–	>5.9	–	0.91
A14	800008 [S2]	–	–	–	–	–	–	–	<3.12	–	<0.40	–	<3.14	–	–	–	–
	800009 [S2]	21:53:32.82	(0.5)	+17:32:22.8	(0.8)	11.24	(4.04)	4.90	15.81	(4.34)	10.97	(3.54)	<4.98	–	>2.20	–	0.83
A15 ¹	800008 [S3]	21:53:33.19	(0.1)	+17:42:10.0	(0.1)	35.17	(6.93)	11.30	36.60	(6.83)	20.15	(5.24)	16.47	(4.38)	1.22	(0.46)	1.76
	800009 [S3]	21:53:33.18	(0.1)	+17:42:09.9	(0.1)	35.34	(6.93)	11.38	40.51	(7.03)	23.19	(5.42)	17.33	(4.49)	1.34	(0.47)	2.04

The exposure times are 9.83 ks for 800008 and 9.13 ks for 800009.

¹ this source is CXOU J215333.2+174209 (source 2) in Fabian et al (2000), source 3 (updated to CXOU J215333.2+174211) in Cowie et al (2001) and source B in Wilman, Fabian & Gandhi (2000).

The counts given by the WAVDETECT algorithm (cols 7 and 8) are for the total 0.5-7 keV band, and differ from the counts given in cols 10 and 11 due to the different background estimation methods (see text for details).

The significance given in column 9 is that obtained from WAVDETECT.

S/H is the ratio of the counts in the 0.5-2 keV band (cols 12 and 13) and those in the 2-7 keV band (cols 14 and 15).

The PSF ratio given in the final column is the ratio of the source size to the PSF size at the source location, as output from the WAVDETECT algorithm.

Sources marked with a * may have their counts in the soft band (and hence the S/H ratio) affected by the proximity to the cluster.

Sources marked with a † are close to the edge of the chip, where dither may affect the counts and S/H ratios.

Table 1. Serendipitous X-ray sources in the field of the cluster A2390 (ctd)

Name	Seq. No. [Chip]	RA _X	Δα _X ($''$)	DEC _X	Δδ _X ($''$)	WAV (cts)	(err)	Significance	0.5-7 keV (cts)	(err)	0.5-2 keV (cts)	(err)	2-7 keV (cts)	(err)	S/H	(err)	PSF ratio
A16	800008 [S2]	21:53:33.57	(0.1)	+17:37:34.7	(0.1)	31.82	(5.72)	15.44	31.59	(5.72)	23.79	(4.95)	7.77	(2.87)	3.06	(1.30)	1.22
	800009 [S2]	21:53:33.62	(0.1)	+17:37:35.2	(0.2)	28.13	(5.37)	13.84	27.33	(5.28)	21.34	(4.64)	5.93	(2.50)	3.60	(1.71)	1.00
A17 ²	800008 [S3] *	21:53:33.79	(0.1)	+17:41:15.1	(0.1)	12.59	(4.24)	5.35	15.61	(4.26)	15.15	(4.13)	<2.02	–	>7.49	–	1.65
	800009 [S3]	21:53:33.71	(0.1)	+17:41:15.3	(0.1)	15.88	(4.90)	6.24	23.77	(5.31)	19.89	(4.81)	<4.50	–	>4.42	–	2.34
A18 ³	800008 [S3]	21:53:33.98	(0.1)	+17:42:41.3	(0.1)	68.73	(9.02)	20.50	71.96	(9.05)	24.52	(5.61)	47.52	(7.11)	0.52	(0.14)	1.43
	800009 [S3]	21:53:33.95	(0.1)	+17:42:41.2	(0.1)	71.68	(9.01)	22.84	76.51	(9.14)	29.69	(5.86)	46.88	(7.02)	0.63	(0.16)	1.41
A19	800008 [S2]	21:53:34.78	(0.1)	+17:36:30.5	(0.1)	113.97	(10.77)	49.44	115.39	(10.77)	79.65	(8.95)	35.61	(5.99)	2.24	(0.45)	1.22
	800009 [S2]	21:53:34.84	(0.1)	+17:36:30.8	(0.1)	123.53	(11.25)	49.88	127.53	(11.35)	95.34	(9.81)	31.80	(5.67)	3.00	(0.62)	1.35
A20	800008 [S3]	21:53:40.77	(0.1)	+17:44:15.4	(0.1)	149.74	(12.44)	54.56	153.88	(12.48)	61.98	(7.95)	92.49	(9.65)	0.67	(0.11)	1.27
	800009 [S3]	21:53:40.76	(0.1)	+17:44:15.6	(0.1)	136.48	(11.82)	54.39	139.67	(11.87)	61.97	(7.91)	78.06	(8.86)	0.79	(0.14)	1.51
A21	800008 [S3]	–	–	–	–	–	–	–	10.34	(3.58)	6.06	(2.73)	<4.64	–	>1.31	–	–
	800009 [S3]	21:53:40.93	(0.4)	+17:45:21.1	(0.4)	7.98	(3.54)	3.74	10.81	(3.70)	9.56	(3.40)	<2.92	–	>3.27	–	1.02
A22	800008 [S1] †	21:53:43.78	(0.7)	+17:29:10.6	(0.9)	38.81	(8.15)	10.93	59.23	(8.55)	52.66	(7.62)	<8.00	–	>6.58	–	1.07
A23	800008 [S3] *	21:53:44.47	(0.8)	+17:42:58.4	(0.4)	4.87	(4.98)	3.47	13.26	(4.81)	9.48	(4.10)	3.78	(2.52)	2.51	(1.99)	4.27
	800009 [S3]	–	–	–	–	–	–	–	<7.95	–	<6.8	–	<4.12	–	–	–	–
A24	800008 [S3]	21:53:45.55	(0.2)	+17:41:47.7	(0.1)	29.40	(6.49)	9.75	31.59	(6.37)	13.61	(4.45)	19.14	(4.67)	0.71	(0.29)	2.46
	800009 [S3]	21:53:45.54	(0.1)	+17:41:47.3	(0.1)	14.77	(4.16)	6.61	15.65	(4.18)	8.18	(3.04)	7.49	(2.87)	1.09	(0.58)	1.19
A25	800009 [S3]	21:53:46.31	(0.3)	+17:46:26.6	(0.3)	45.03	(7.26)	15.54	49.25	(7.19)	44.83	(6.79)	<4.70	–	>9.54	–	1.58
A26	800008 [S2] †	21:53:47.98	(0.3)	+17:37:56.2	(0.4)	13.57	(3.83)	6.58	13.42	(3.84)	11.83	(3.54)	<2.08	–	>5.69	–	1.67
	800009 [S2]	21:53:47.96	(0.1)	+17:37:55.6	(0.2)	34.66	(5.98)	16.40	36.12	(6.07)	29.85	(5.51)	6.14	(2.53)	4.86	(2.19)	0.98
A27	800008 [S3]	21:53:47.97	(0.2)	+17:42:47.6	(0.2)	23.45	(5.01)	10.80	23.08	(4.91)	15.94	(4.09)	7.17	(2.71)	2.23	(1.02)	1.08
	800009 [S3]	21:53:47.97	(0.1)	+17:42:47.2	(0.1)	35.29	(6.02)	17.05	52.96	(7.34)	45.83	(6.82)	7.10	(2.70)	6.45	(2.63)	0.90
A28	800008 [S3]	21:53:48.84	(0.1)	+17:41:59.8	(0.2)	31.27	(5.78)	13.78	30.67	(5.70)	24.96	(5.11)	5.70	(2.52)	4.38	(2.13)	1.01
	800009 [S3]	21:53:48.85	(0.2)	+17:41:60.2	(0.2)	13.28	(4.07)	5.86	14.06	(4.08)	10.79	(3.53)	<4.10	–	>2.63	–	1.66
A29	800008 [S3]	21:53:52.85	(0.4)	+17:44:02.2	(0.3)	11.24	(3.59)	5.35	11.67	(3.60)	8.01	(2.93)	<4.20	–	>1.91	–	0.95
A30	800008 [S3]	21:53:53.61	(0.5)	+17:44:02.4	(0.7)	10.51	(3.75)	4.75	11.40	(3.76)	<4.66	–	7.36	(2.97)	<1.06	–	1.51
A31	800008 [S3]	21:53:55.00	(0.2)	+17:43:59.2	(0.6)	10.03	(3.46)	4.76	11.81	(3.62)	10.28	(3.29)	<3.02	–	>3.40	–	0.96

² this source is CXOU J215333.8+174113 (source 3) in Fabian et al (2000) and source 2 (updated to CXOU J215333.8+174116) in Cowie et al (2001).³ this source is CXOU J215334.0+174240 (source 3) in Fabian et al (2000), source A in Wilman et al (2000) and source 1 (updated to CXOU J215334.0+174242) in Cowie et al (2001).

Table 2. A 2390 Observations

Band	Date	Telescope & Instrument	Plate Scale (arcsec/pixel)	Filters	Seeing (arcsec)	Typical Exposure (seconds)
B	1994 Dec 08	WHT Prime Focus	0.421	Kitt Peak 1	3.8	500
R	1994 Jun 06	INT Prime Focus	0.590	Kitt Peak 3	1.6	600
I	1994 Dec 08	WHT Prime Focus	0.421	Kitt Peak 1	1.4	300
I	1990 Oct 16	CFHT focam	0.205	CFHT #1809	0.7	700
J, H, K	2000 Aug 10/11	UKIRT UFTI	0.091	J98, H98, K98	0.6	540

Table 3. A 2390 Photometry

Object	RA _{opt}	Dec _{opt}	B	R	I	J	H	K	Aperture diameter (arcsec)
A3	21:52:55.80	17:44:34.1	>22.5 ^D	>21.0 ^D	–	–	–	–	–
A4	21:53:00.95	17:44:52.4	22.0±0.5 ^D	>21.0 ^D	–	–	–	–	–
A5	21:53:04.92	17:38:33.8	16.89 ^A	14.80 ^A	–	–	–	–	–
A6	21:53:20.72	17:41:19.6	>22.5 ^D	21.96±0.10	–	–	–	–	4.5
A7	–	–	>22.5 ^D	>23.40	>22.25	–	–	–	4.5
A8	21:53:23.86	17:39:30.3	23.69±0.37	21.84±0.08	20.24±0.06	19.50±0.06	18.38±0.04	17.42±0.03	4.5
A9 ^A	21:53:23.68	17:30:19.9	13.31 ^A	12.05 ^A	–	–	–	–	–
A10	21:53:25.30	17:43:22.3	22.39±0.09	19.91±0.03	19.01±0.03	–	–	–	4.5
A11 ^D	21:53:26.47	17:35:17.4	22.0±0.5 ^D	>21.0 ^D	–	–	–	–	–
A12 ^P	21:53:29.05	17:48:54.7	>22.5 ^D	>21.0 ^D	–	19.48±0.05	18.35±0.03	17.70±0.03	4.5
A14	21:53:32.86	17:32:23.8	>22.5 ^D	>21.0 ^D	–	18.32±0.03	17.59±0.03	16.78±0.02	4.5
A15 ^S	21:53:33.22	17:42:10.4	>23.72	>23.25	>22.88‡	>21.71	20.07±0.06	18.83±0.04	4.5
A16	21:53:33.65	17:37:35.6	22.0±0.5 ^D	20.98±0.06	–	19.82±0.07	19.55±0.10	18.90±0.10	2.7
A17	21:53:33.75	17:41:15.8	>23.66	22.99±0.24	21.11±0.10‡	19.38±0.03	18.59±0.03	17.58±0.02	2.7
A18	21:53:33.99	17:42:41.6	>23.74	23.86±0.37	21.13±0.11‡	18.65±0.03	17.57±0.02	16.49±0.02	4.5
A19	21:53:34.88	17:36:31.7	20.50±0.30 ^A	19.35±0.03	–	18.74±0.03	17.80±0.03	17.37±0.03	4.5
A20	21:53:40.80	17:44:16.0	21.90±0.07	20.18±0.03	19.38±0.02	18.22±0.02	17.64±0.02	16.43±0.02	4.5
A21	21:53:40.97	17:45:21.6	>22.5 ^D	>23.34	–	–	–	–	4.5
A22 ^D	21:53:43.87	17:29:12.3	20.48 ^A	20.5±0.5 ^D	–	–	–	–	–
A23	–	–	>23.67	>23.89	>22.49	–	–	–	2.7
A24	21:53:45.58	17:41:47.8	20.26±0.04	18.24±0.02	17.41±0.03	16.31±0.02	15.63±0.02	14.90±0.02	4.5
A25	21:53:46.35	17:46:27.0	20.20 ^A	17.76 ^A	–	–	–	–	–
A26	21:53:48.00	17:37:56.1	20.10 ^A	19.85±0.03	–	–	–	–	4.5
A27	21:53:47.98	17:42:48.0	21.97±0.09	20.91±0.05	19.22±0.04	18.97±0.04	18.42±0.04	17.62±0.03	2.7
A28	21:53:48.87	17:42:00.0	22.20±0.10	21.30±0.08	20.58±0.05	18.98±0.03	18.19±0.03	17.21±0.02	4.5

The following sources are not included in the table as they are not in the field of view of the archival optical datasets, and there is no obvious id in either the DSS B or R images: A1 A2, A29, A30 and A31.

The RA_{opt} and Dec_{opt} listed in columns 2 and 3 are from Barger (private communication); except for those sources whose name is marked by ^A or ^D where the position is from the APM or DSS data respectively.

In columns 4 and 5, a magnitude (or upper limit) marked by a ^D or ^A was estimated from the DSS (second-generation) image, or from the Palomar Observatory Sky Survey as scanned from the APM at Cambridge, as the source was not in the field of view of the archival optical data. The remaining magnitudes are either from the INT (*R*-band), or the WHT (*I*- and *B*-band) image, except for the three *I*-band magnitudes marked ‡, which were measured from the deeper CFHT image.

The source marked ^P has a systematic photometric uncertainty of 14% in J, 12% in H and 8% in K. The value stated has been calibrated against all standards observed through the night - see text.

The aperture size stated in the last column is for the infra-red data. For the optical data, the seeing-corrected apertures were typically larger.

The source marked ^S also has ISO 6.7- and 15- μm detections of 110 and 350 μJy respectively (Lémonon et al 1998). These translate to magnitudes of 14.8 and 12.7.

Table 4. Equivalent widths of emission lines, in Å.

Source	CIII] λ 1909	MgII λ 2798	FWHM of Mg II (km s ⁻¹)	[OII] λ 3727	H β	[OIII] λ 5007	H α	[NII] λ 6584	[SII] λ 6731
A4	–	21.2 \pm 1.0	4202 \pm 226	1.7 ^{+1.2} _{-1.1}	–	–	–	–	–
A6	–	35.6 ^{+2.3} _{-2.2}	6995 \pm 465	9.1 ^{+1.5} _{-1.4}	–	–	–	–	–
A8	–	<2.5	–	24.8 \pm 0.7	15.2 ^{+1.1} _{-1.2}	27.9 \pm 2.0	–	–	–
A10	–	–	–	–	–	–	0.9 \pm 0.5	5.4 ^{+0.6} _{-0.5}	–
A13	33.6 ^{+1.8} _{-1.7}	49.6 ^{+2.4} _{-2.3}	8455 \pm 139	–	–	–	–	–	–
A16	25.2 ^{+2.2} _{-2.0}	33.9 ^{+2.5} _{-2.4}	8203 \pm 453 [†]	–	–	–	–	–	–
A18	–	–	–	13.5 ^{+3.1} _{-2.7}	–	–	–	–	–
A19	30.7 \pm 1.4	45.6 \pm 1.9	8271 \pm 403 [†]	–	–	–	–	–	–
A20	–	–	–	163.6 \pm 6.1	71.1 ^{+7.2} _{-7.3}	711.8 ^{+26.1} _{-25.7}	249.3 ^{+11.7} _{-11.3}	53.5 ^{+6.5} _{-6.6}	10.7 \pm 6.2
A24	–	–	–	–	–	35.1 \pm 1.6	18.7 ^{+1.0} _{-0.9}	32.2 ^{+1.5} _{-1.0}	2.7 \pm 0.8
A26	24.2 \pm 1.2	23.0 \pm 0.7	3825 \pm 126	–	–	–	–	–	–
A28	–	79.2 \pm 3.7	6089 \pm 277	–	–	–	–	–	–

[†] For A16 and A19, the MgII line is fit better by a double Gaussian, whereas the equivalent width and velocity width listed in the table are from a single Gaussian fit. In A16 these two components have velocity widths of 2020 \pm 239 and 10593 \pm 516 km s⁻¹, with the broader component having \sim 6 times the intensity of the narrow line. In A19 the two components have velocity width 3548 \pm 503 and 12933 \pm 679 km s⁻¹, and the broader component is \sim 7 times the intensity of the narrow line.

Table 5. A 2390 Redshifts

Source	$z_{\text{spectroscopic}}$	$z_{\text{photometric}}$ (90% confidence)	Reduced χ^2 (d.o.f.)	Galaxy Type	Age (Gyr)	A_V	M_B	$z_{\text{secondary}}$
A4	1.2172	–	–	–	–	–	–	–
A6	1.0690	–	–	–	–	–	–	–
A8	0.8030	0.79 (0.75,0.82)	1.98 (5)	Burst	0.36	0.60	-22.44	4.33
A10	0.2242	–	–	–	–	–	–	–
A12 ^P	–	2.28 (1.67,3.33)	0.04 (4)	Burst	0.26	0.30	-24.98	0.63
A13	1.5933	–	–	–	–	–	–	–
A14	–	1.35 (0.89,1.80)	0.04 (4)	Burst	0.72	0.00	-24.47	5.29
A15	2.6 ^{C3}	2.78 (2.07,3.34)	0.19 (6)	E	1.43	1.80	-21.44 [‡]	3.16
A16	1.6321	1.35 (1.17,2.06)	1.08 (4)	QSO	0.04 [†]	0.30	-23.25	0.36
A17	1.466 ^{C2}	1.11 (0.99,1.15)	0.39 (5)	Burst	0.51	0.60	-21.77 [‡]	4.63
A18	1.467 ^{C1}	1.45 (1.31,1.53)	2.02 (5)	Burst	2.60	0.00	-23.20 [‡]	5.72
A19	1.6750	0.52 (0.42,0.60)	2.02 (4)	E	0.26	0.00	-22.99	3.09
A20	0.305	0.22 (0.18,0.38)	1.40 (5)	CWW Scd with AGN	2.60 [†]	0.60	-19.57	0.33
A24*	0.214	0.26 (0.15,0.52)	0.42 (5)	E	4.5	0.00	-22.02	0.47
A26	1.5187	–	–	–	–	–	–	–
A27	–	0.87 (0.82,0.92)	5.15 (5)	Burst	0.18	0.00	-23.62	0.54
A28	1.0330	1.21 (1.15,1.33)	0.19 (5)	S0	0.72	0.90	-23.61	1.63

M_B in column 8 is the absolute Vega Magnitude in the B Bessell filter. Those sources with a magnitude marked by a ‡ have been corrected for the magnification due to gravitational lensing.

^{C1} This is a spectroscopic redshift from Cowie et al (2001).

^{C2} This is a spectroscopic redshift from Cowie et al (2001) based on the single identification of a line, but also consistent with their photometric redshift estimate of 1.5 \pm 0.2. A different identification would imply a redshift of 2.317 instead.

^{C3} This is a photometric redshift of 2.6^{+0.1}_{-0.2} from Cowie et al (2001).

^P There is a high degree of degeneracy between this redshift estimate and the secondary solution, with small changes in the photometry. See text for details.

* This source is identified as an Sbc galaxy with a redshift of $z = 0.21501$ by Yee et al (1991). A fit to an Sbc template gives $z_{\text{phot}} = 0.3$.

† This is a Coleman et al (1980; CWW), observed, fixed-age SED. The age has been determined by associating with a Bruzual-Charlot synthetic spectrum with redshift and reddening fixed to the values stated.

Table 6. Fits to the X-ray spectra of the brighter sources

Source	Γ	ΔN_{H} (10^{22} cm^{-2})	Reduced χ^2 (d.o.f.)	L(2-10 keV) ($10^{44} \text{ erg s}^{-1}$)	notes
A6 †	$2.1^{+1.0}_{-0.6}$	<0.61	0.77 (13)	9.2	
A15	$1.7^{+2.0}_{-1.4}$	$17.5^{+60}_{-17.5}$	0.65 (9)	13.0*	
	[2]	$21.9^{+36}_{-14.6}$	0.60 (10)	17.0*	
A16	$1.3^{+2.6}_{-1.3}$	$0.2^{+12.8}_{-0.16}$	0.96 (6)	2.9	
	[2]	$3.8^{+8.0}_{-3.8}$	0.92 (7)	3.9	
A18	$3.2^{+1.3}_{-0.5}$	34.7^{+20}_{-14}	0.57 (11)	60.0*	
	[2]	$20.4^{+7.1}_{-5.2}$	0.81 (12)	20.0*	
A19	$2.31^{+0.5}_{-0.4}$	$2.6^{+2.1}_{-1.6}$	0.91 (19)	13	
A20	$1.2^{+0.2}_{-0.3}$	$1.5^{+0.9}_{-0.6}$	0.53 (30)	1.0	
	[2]	$2.7^{+0.7}_{-0.6}$	0.71 (31)	1.0	
A24	$1.3^{+3.8}_{-1.7}$	$1.8^{+4.9}_{-1.8}$	0.60 (8)	0.1	fit to 800008 data only
	[2]	$2.9^{+2.8}_{-1.4}$	0.57 (9)	0.1	fit to 800008 data only
A26	$4.2^{+5.8}_{-2.3}$	$3.9^{+12}_{-3.9}$	0.92 (2)	4.8	fit to 800009 data only
	[2]	< 1.9	1.42 (3)	3.0	fit to 800009 data only

L(2-10 keV) is the unabsorbed 2-10 keV luminosity.

A square bracket around the value of Γ in column 2 denotes that the parameter was fixed at this value.

† The count rates for A6 (see Table 1) suggest the source is softer in the 800009 observation. Separate spectral fits to each spectrum suggest that this may be due to a change in N_{H} , but since the errors on the separate fits overlap we present the results here only for joint fitting.

* Sources A15 and A18 lie behind the cluster, and the luminosities listed are not corrected for the magnification factors of 7.8 and 2.1 respectively (Cowie et al 2001).

Table 7. Absorbed-powerlaw-model-predicted intrinsic columns or photon indices from the observed S/H ratio for sources with insufficient counts for spectral fitting

Source	Redshift	S/H ratio	Prediction ¹
A4	1.2172	> 1.89	$N_{\text{H}} < 5$ [2.0] $N_{\text{H}} < 0.5$ [1.4]
A8	0.8030	> 4.71 [‡]	$N_{\text{H}} < 0.1$ [2.0] and $\Gamma > 1.4$
A10	0.2242	> 31.26	$\Gamma > 3$
A12 ²	2.28	2.03 ± 1.1	$1 < N_{\text{H}} < 30$ [2.0] $N_{\text{H}} < 20$ [1.4] or* $\Gamma > 1.4$
A12 ²	0.66	2.03 ± 1.1	$0.2 < N_{\text{H}} < 4$ [2.0] $N_{\text{H}} < 2$ [1.4] or* $\Gamma > 1.4$
A13	1.5933	> 5.9	$\Gamma > 2$
A14	1.35	> 2.20	$N_{\text{H}} < 5$ [2.0] and $\Gamma > 1.4$
A17	1.466	> 4.42 [‡]	$N_{\text{H}} < 0.5$ [2.0] and $\Gamma > 1.4$
A27	0.87	2.23 ± 1.0 [†]	$0.7 < N_{\text{H}} < 4$ [2.0] $N_{\text{H}} < 2$ [1.4] or* $\Gamma > 1.4$
		6.45 ± 2.6 [‡]	$N_{\text{H}} < 0.4$ [2.0] or* $\Gamma > 2.0$
A28	1.0330	4.38 ± 2.1 [†]	$N_{\text{H}} < 2$ [2.0] or* $\Gamma > 2.0$ $N_{\text{H}} < 0.2$ [1.4] or* $\Gamma > 1.4$

Redshifts stated to four decimal places are spectroscopic and the rest are photometric.

¹ The limits on the column densities (stated in units of 10^{22} cm^{-2}) account for the errors on the S/H ratio where available; otherwise have been constrained to the nearest half-decade. The assumed powerlaw-indices(Γ) are stated in square brackets.

² The two rows correspond to the two possible photometric redshifts for this source. See Table 5 and the text.

[†] Obtained from 800008 observation only.

[‡] Obtained from 800009 observation only.

* These two possibilities come from the values of S/H at the extremes of the range encompassed by the S/H-error. The upper-limit on N_{H} corresponds to the lower value of S/H and the lower-limit on Γ corresponds to the higher value of S/H.